PLOS PATHOGENS

Structural basis of the recognition of adeno-associated virus by the neurological system-related receptor carbonic anhydrase IV

Ran Zhang[1,2☯], Yixiao Liu[2☯], Fengxi Yu[3], Guangxue Xu[4], Lili Li[5], Baobin Li[6], Zhiyong Lou[iD][2]*

1 Jinshan Hospital, Institute for Translational Brain Research, Fudan University, Shanghai, China, 2 MOE Key Laboratory of Protein Science, School of Medicine, Tsinghua University, Beijing, China, 3 School of Life Sciences, Tsinghua University, Beijing, China, 4 Department of Pathology, Stanford University School of Medicine, Stanford, California, United States of America, 5 Beijing Institute of Biological Products Company Limited, Beijing, China, 6 Department of Anesthesiology, Zhongshan Hospital, Institute for Translational Brain Research, State Key Laboratory of Medical Neurobiology, MOE Frontiers Center for Brain Science, Fudan University, Shanghai, China

☯ These authors contributed equally to this work.
* louzy@mail.tsinghua.edu.cn

🔓 OPEN ACCESS

Abstract

Carbonic anhydrase IV (Car4) is a newly identified receptor that allows adeno-associated virus (AAV) 9P31 to cross the blood-brain barrier and achieve efficient infection in the central nervous system (CNS) in mouse models. However, the molecular mechanism by which engineered AAV capsids with 7-mer insertion in the variable region (VR) VIII recognize these novel cellular receptors is unknown. Here we report the cryo-EM structures of AAV9P31 and its complex with *Mus musculus* Car4 at atomic resolution by utilizing the block-based reconstruction (BBR) method. The structures demonstrated that Car4 binds to the protrusions at 3-fold axes of the capsid. The inserted 7-mer extends into a hydrophobic region near the catalytic center of Car4 to form stable interactions. Mutagenesis studies also identified the key residues in Car4 responsible for the AAV9P31 interaction. These findings provide new insights into the novel receptor recognition mechanism of AAV generated by directed evolution and highlight the application of the BBR method to studying the virus-receptor molecular mechanism.

Author summary

Recombinant adeno-associated viruses (AAVs) are promising vectors for gene therapy, especially for metabolic, neurological and hematological diseases. Among them, AAV9P31, which was designed based on the AAV9 backbone, is a highly effective candidate for gene delivery in the central nervous system. To optimize this vector, it is crucial to understand how AAV9P31 recognizes its receptor carbonic anhydrase IV (Car4) and crosses the blood-brain barrier. In this study, we determined the atomic structures of AAV9P31 in its native state and in complex with Car4, revealing the molecular details of virus-receptor interactions. Moreover, we applied the block-based reconstruction

algorithm to capture the asymmetric binding of the receptor on the icosahedral virus, which is important for studying recombinant AAV targeting neurological receptors.

Introduction

Adeno-associated viruses (AAVs) are a type of single-stranded DNA virus within the *Parvoviridae* family [1]. Because of the broad differences in their tissue tropism and the absence of pathology, AAVs considered promising vectors for therapeutic gene delivery [1,2]. To date, Luxturna, Zolgensma, Elevidys and Roctavian have been approved by the FDA for the treatment of hereditary retinal dystrophy, spinal muscular atrophy, Duchenne muscular dystrophy and haemophilia A, respectively [3–7]. The application of AAV vectors to treat neurological diseases has recently attracted particular interest [8,9]; however, the delivery of exogenous genes by AAV vectors across the blood–brain barrier (BBB) and into the central nervous system (CNS) is a major challenge limiting the development of AAV-based therapeutics targeting the CNS system.

Several strategies for AAV capsid evolution have been developed to achieve higher efficiency in crossing the BBB. For example, a Cre recombination-based AAV targeted evolution (CREATE) method was applied to yield AAV9 variants with enhanced CNS transduction in mouse brain, e.g. AAV-PHP.B and AAV-PHP.eB [10]. These variants have an inserted peptide between amino acids Q588 and A589 in the variable region (VR) VIII of wild-type (wt) AAV9 VP3 [10,11]. Recently, a tropism redirection of AAV by cell-type-specific expression of RNA (TRACER) method for AAV evolution was developed based on the recovery of bulk capsid library RNA expressed in a cell-type-specific manner from nontransgenic animal tissue [12]. Among the generated AAV9 variants with higher efficiency for infecting the CNS, the variant AAV9P31, which includes an additional sequence (WPTSYDA) inserted between Q588 and A589 of the wt AAV9 VP3 VR-VIII, exhibited efficient CNS tropism with 385-fold higher EGFP expression in the mouse CNS and 1000-fold higher EGFP expression in the mouse spinal cord compared to wt AAV9 [12].

The specific receptor is a key determinant for AAV infection. Adeno-associated virus receptor (AAVR), a glycosylated protein containing five polycystic kidney disease (PKD) repeat domains (PKD1-5) [13], was first identified as a protein receptor for multiple AAV serotypes [14]. AAVR interacts with AAV1/2 by PKD2 contacting the spike of the AAV1/2 capsid, whereas AAVR binds with AAV5 by PKD1 lying on the plateau region of the AAV5 capsid [15,16]. Moreover, the GPI-linked protein LY6A was reported to play an essential role in AAV-PHP.B/PHP.eB crossing the BBB in selected mouse models [17–19]. A structural analysis revealed that one LY6A molecule binds at the icosahedral 3-fold axis of the AAV-PHP.B/PHP. eB particles, in which three VP3 capsomers clamp one LY6A [20]. Although the structural study revealed that the footprint of LY6A was associated with the inserted peptide in AAV-PHP.B/PHP.eB VP3 VR-VIII, icosahedral averaging within cryo-EM reconstruction resulted in only a block density at the icosahedral 3-fold axis instead of a traceable density for the polypeptide of LY6A [20].

A very recent work showed that the GPI-linked protein carbonic anhydrase IV (Car4) is an essential receptor for AAV9P31 and AAV9P36 crossing the BBB in a mouse model [21]. Car4 is localized on the luminal surface of brain endothelial cells throughout the cortex and cerebellum, and its sequence and structure are conserved in *Mus musculus* and *Homo sapiens* [22–25]. Biochemical results and structure prediction suggested that Car4 binds at the icosahedral 3-fold axis [21]. However, the molecular details of the AAV9P31-Car4 interaction remain

unclear. In this paper, we report the atomic structures of AAV9P31 and the AAV9P31-Car4 complex by employing an improved block-based reconstruction method [26] to dissect the mechanism of the recognition of AAV9P31 by Car4. By combining mutagenesis studies, we have successfully identified key residues within the interfaces. This discovery serves as a foundation for further modifications of AAV9P31, potentially enabling its application in therapeutics for human neurological diseases.

Results

Structure of AAV9P31

The structure of AAV9P31 was determined by cryo-EM with a final resolution of 1.76 Å at a 0.143 cutoff of Fourier shell correlation (FSC) (S1A and S1B Fig, and S1 Table), and the side chains of VP3 capsomers were generally well defined (S2A–S2D Fig). The overall architecture of AAV9P31 and wt AAV9 (PDB: 7WJW) [20] share high similarities on most of the surface regions (with a root-mean-square deviation (RMSD) of 0.569 Å across all Cα atoms in VP3 residues), including a channel-like structure at the five-fold axes, a depression at the twofold axes and three protrusions surrounding each threefold axis (Fig 1A and 1B). The major difference is found in the VP3 VR-VIII region (S3A Fig). AAV9P31 has an additional seven inserted
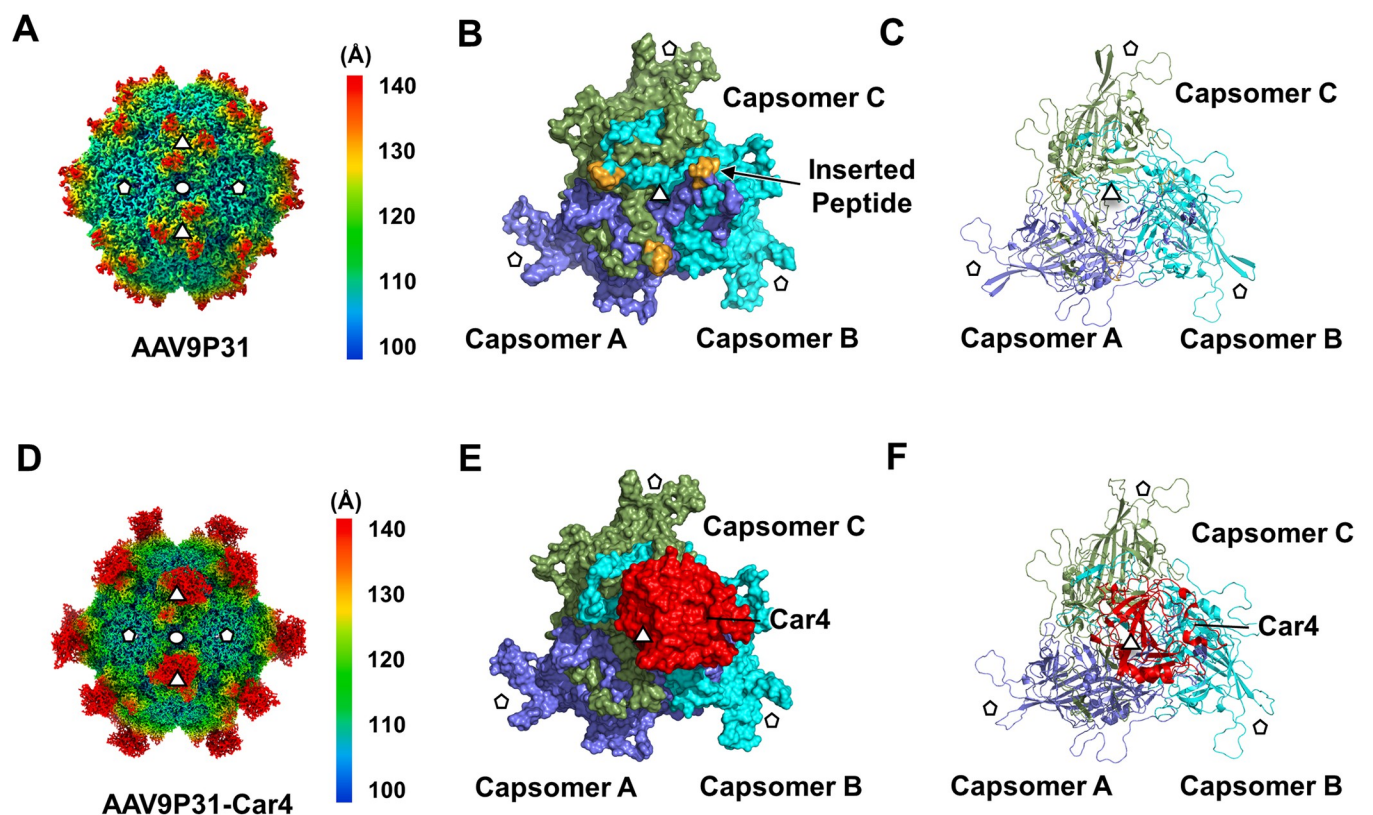
Fig 1. Cryo-EM reconstruction of AAV9P31 and AAV9P31-Car4. (**A**) The reconstructed cryo-EM map of AAV9P31. The radial distance color scheme is used to indicate the density (<100 Å: blue; 110–130 Å: from cyan to yellow; >140 Å: red). (**B**) The trimer of AAV9P31 VP3 in the threefold axis is colored by surface. (**C**) Cartoon representations of (**D**). The inserted peptide of AAV9P31 is colored bright orange in (**B**) and (**C**). (**D**) Overall cryo-EM map of the AAV9P31-Car4 complex. The radial distance color scheme is used to indicate the density by color (<100 Å: blue; 110–130 Å: from cyan to yellow; >140 Å: red). (**E**) The trimer of AAV9P31-Car4 in the threefold axis is colored by surface. (**F**) Cartoon representations of (**E**). Capsomer A is colored slate blue; capsomer B is colored cyan; capsomer C is colored smudge green; Car4 is colored red (**B, C, E, F**). The 5-, 3- and 2-fold icosahedral axes of symmetry are indicated with a pentagon, triangles, and an oval, respectively (**B, C, E, F**).

residues (WPTSYDA) between AAV9 VP3 Q588 and D589, which are numbered 588a to 588g (S3B Fig). The main chain of the inserted peptide W588a-A588g is well defined in the density map (S3C Fig).

Block-based reconstruction (BBR) algorithm for reconstructing the AAV9P31-Car4 complex

To determine the binding details of Car4 on AAV9P31, AAV9P31 particles were incubated with purified Car4 (amino acids W22 to S277) for 5 minutes before cryo-EM sampling and data collection. In the 2D and 3D classification, additional density was found at the icosahedral three-fold axis compared to the native AAV9P31, indicating the binding of Car4 to AAV9P31 (Fig 2A). The initial cryo-EM single particle reconstruction was applied with icosahedral symmetry and yielded a final cryo-EM map with a resolution of 1.76 Å at an FSC cutoff of 0.143 (Figs 2B, S1C and S1D). Similar to a previous report of LY6A-AAV-PHP.B/PHP.eB study, additional densities were present at the icosahedral three-fold axis of the AAV9P31 capsid upon Car4 incubation (Figs 2B and S4). However, the current reconstruction strategy imposing icosahedral symmetry still failed to obtain the structure of Car4 at near-atomic resolution. In conventional algorithms for reconstructing an icosahedron, the three-fold axes are typically treated as three identical symmetric modules. Nevertheless, if a three-fold axis can only associate with an asymmetric receptor protein, the restoration of the three-fold axis deviates from the established symmetry. Consequently, achieving a three-dimensional reconstruction of the receptor density for the entire particle during icosahedron reconstruction becomes unattainable. Instead, computations must be conducted independently on each three-fold axis, treating them as sub-particles.

To overcome the aforementioned obstacle, we employed an improved block-based reconstruction (BBR) algorithm to calculate the receptor bound at the icosahedral axes (S5 Fig). The BBR method was developed by the group of Xinzheng Zhang [27]. In this method, large object can be split into smaller blocks by symmetry expansion so that sub-particles can be reconstructed and refined by single particle algorithms [27]. In total, 13,604,676 subparticles at the icosahedral three-fold axes were extracted by symmetry expansion of the particles (S5B Fig). After extracting all sub-particles from the micrographs, they were classified into sixteen classes. Five of sixteen classes showed clear signals of bound Car4, one of sixteen exhibited fuzzy noise at the position binding Car4, and the other 10 classes showed signals for VP3 alone (S5C Fig). The classes with Car4 signals are similar but have 120° rotations between them (Figs 2D and S5D–S5F). There are 2,067,911 particles in the 5 classes with the Car4 signal (15.2% of all extracted particles), indicating that each AAV9P31 virion binds only three Car4s on average. The final resolution of the three-fold axis block is 2.28 Å at 0.143 cutoff of FSC (S1E and S1F Fig).

Overall structure of the AAV9P31-Car4 complex

In the structure of AAV9P31-Car4, Car4 asymmetrically interacts with the protrusion of three VP3 capsomers protruding at the icosahedral 3-fold axes (Figs 1D–1F and 2C). The binding pattern is totally different from that in our previously reported AAV9-AAVR complex (PDB: 7WJX; EMD-32551), which has three AAVRs binding at the virus three-fold axes [20]. For easy representation, we named the VP3 capsomers at the 8, 4 and 12 o'clock positions capsomers A, B and C, respectively (Fig 2C). The 3D classification in BBR shows that the bound Car4 has major contacts with two capsomers, either A/B, B/C or C/A, with very similar ratios (5.11%, 5.06% and 4.89%) and conserved binding behaviors in the three BBR groups (Figs 2D and S5D–S5F). Given that the BBR groups have 120-degree rotational symmetry about the 3-fold axis, we use the group in which Car4 interacts with capsomer A/B to represent the other
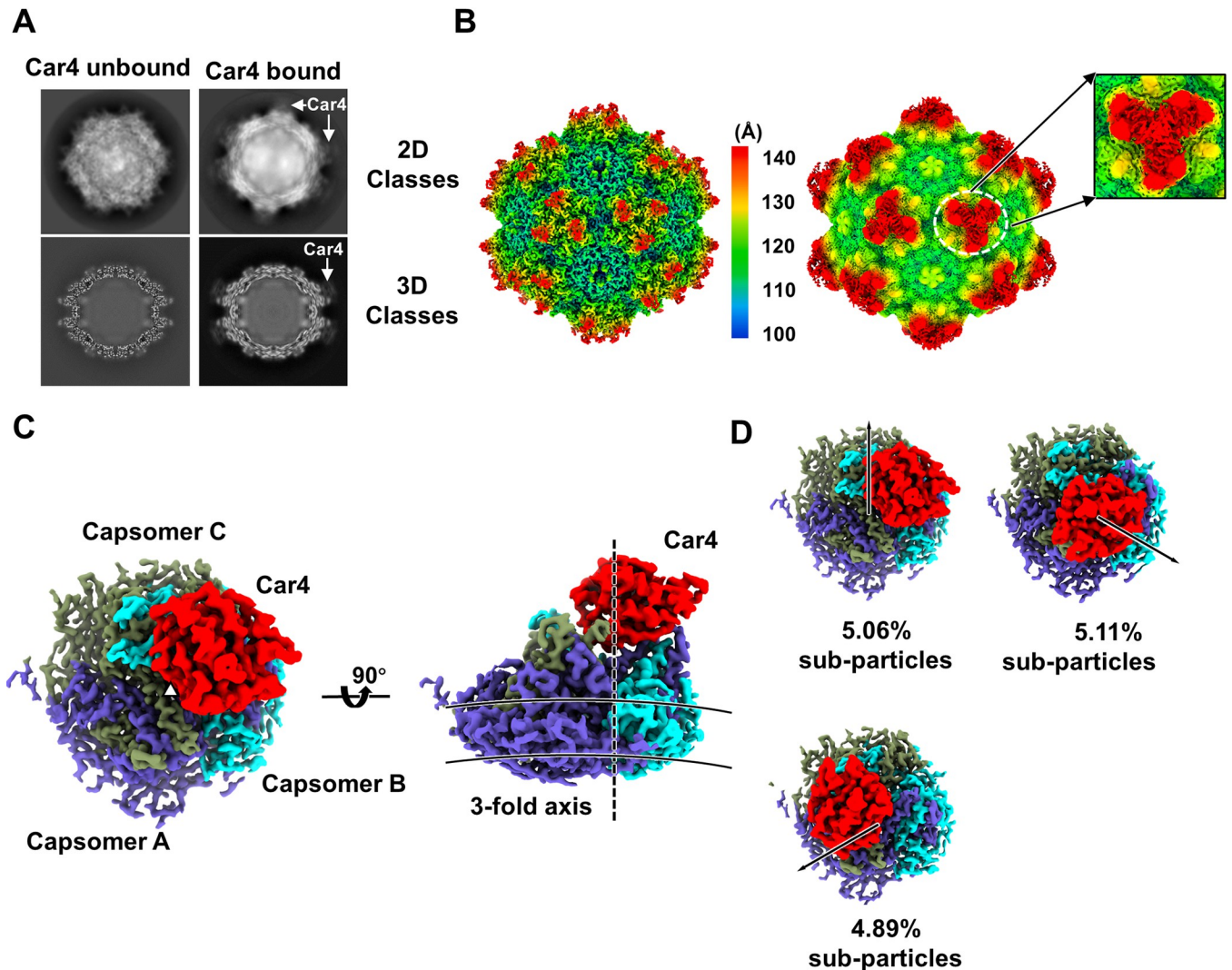
Fig 2. Block-based reconstruction of the 3-fold axis of AAV9P31-Car4. (A) 2D and 3D classification of the unbound and bound states of AAV9P31. The density of Car4 is indicated by a white arrowhead. The box size is 440 pixels, and the pixel size is 0.8433 Å. **(B)** Density map of icosahedral reconstructed AAV9P31-Car4 (unsharpened) shown by counter levels of 2.8σ (left) and 0.5σ (right). The magnified figure of the white circle shows the fuzzy electron density of Car4. The radial distance color scheme is used to indicate the density by color (<100 Å: blue; 110–130 Å: from cyan to yellow; >140 Å: red). **(C), (D)** Density of three-fold axis blocks isolated from the AAV9P31-Car4 map. The icosahedral three-fold axis is indicated at its approximate position by the dotted line. The top view and side view are shown in **(C)**. The approximate inner and outer boundaries of the shell are marked by two solid arcs. Three classes of reconstructed blocks are shown in **(D)**. Capsomer A is colored slate blue; capsomer B is colored cyan; capsomer C is colored smudge green; and Car4 is colored red **(C, D)**.

two groups (Fig 1D–1F). Among the two interacting capsomers, capsomer A contributes the major interacting regions with the bound Car4 (Fig 3A–3C and S2 Table). The inserted peptide of capsomer A deeply inserted into the catalytic pocket of the bound Car4. Notably, the Car4 residues spanning $L145_{Car4}$-$D154_{car4}$, which were not identified in the previous work [23], can be clearly defined in the density (S6 Fig).

Interactions of AAV9P31 with Car4

In AAV9P31-Car4 complex, the contact surface on Car4 is 1926.2 Å^2 compared to its entire 23,459 Å^2 accessible surface, indicating a strong virus-receptor interaction. The residues of
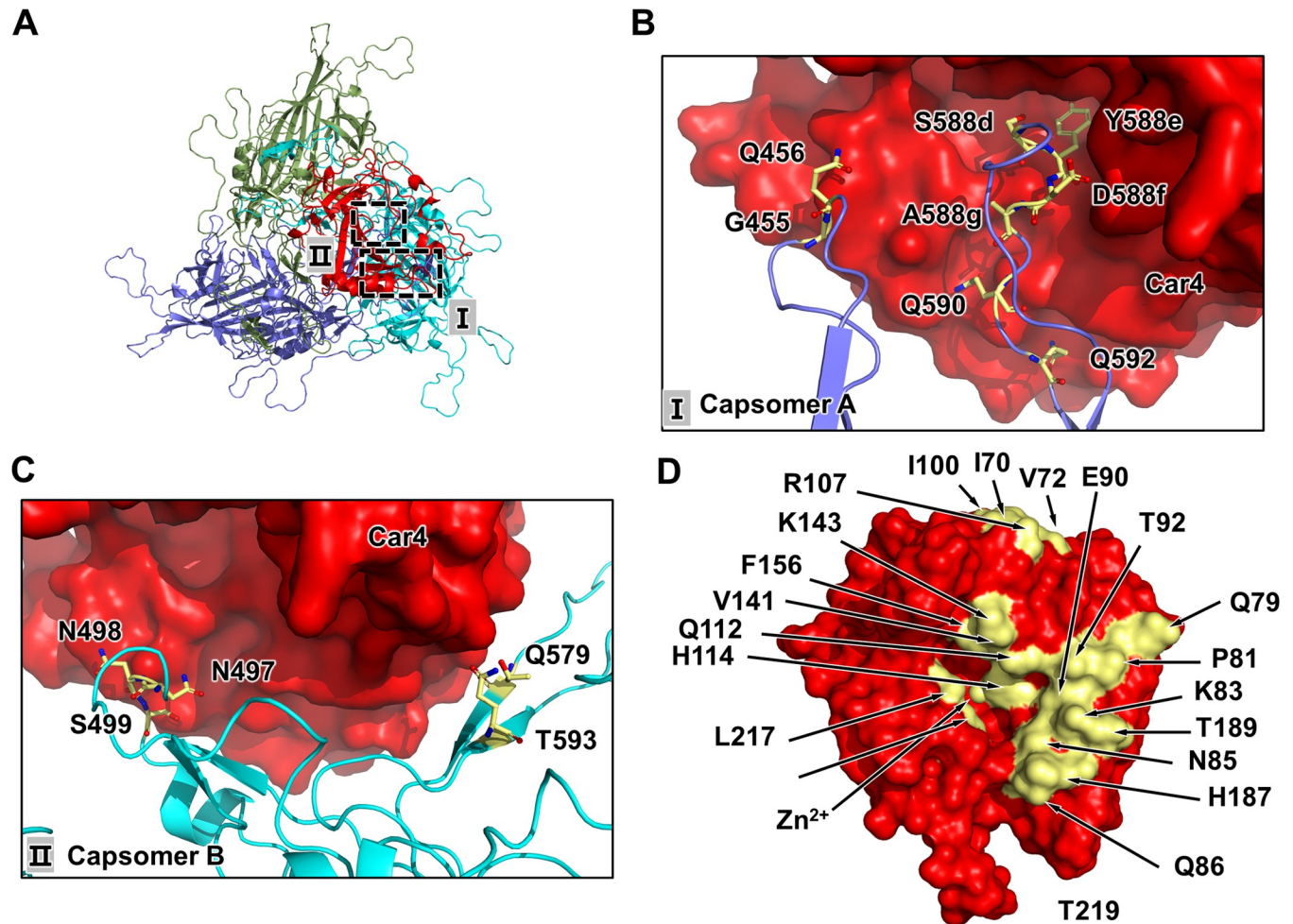
Fig 3. Interactions between AAV9P31 and Car4. (**A**) Cartoon representation of trimeric AAV9P31 capsomers in complex with Car4 from the top view. (**B**) and (**C**) Views of the binding interfaces of capsomer A and capsomer B, with residues that contact Car4 indicated. Car4 is shown on the surface; capsomers A, B or C are shown as cartoons; residues involved in the interfaces are shown in stick representation. (**D**) The residues in Car4 at the interfaces. The residues are indicated and shown in yellow. The letters on the Car4 surface are presented in bold white, and others are presented in bold black. AAV9P31 capsomers A and B are colored in slate blue and cyan, respectively. Bound Car4 is shown in red. Residues at the interfaces are shown in yellow.

https://doi.org/10.1371/journal.ppat.1011953.g003

Car4, including $I70_{Car4}$, $V72_{Car4}$, $Q79_{Car4}$, $P81_{Car4}$, $K83_{Car4}$, $N85_{Car4}$, $Q86_{Car4}$, $E90_{Car4}$, $T92_{Car4}$, $G94_{Car4}$, $Q112_{Car4}$, $V141_{Car4}$, $F156_{Car4}$, $H187_{Car4}$, $T189_{Car4}$, $L217_{Car4}$ and $T219_{Car4}$, were found to be involved in the interaction with AAV9P31, as analyzed by the contact program in the CCP4 suite (distance cutoff of 4.0 Å) [28] (Fig 3D and S2 Table). The interfaces are well defined in the density (S7 Fig)

The interacting residues of AAV9P31 are located on the protrusions and ridges of capsomers A/B near the icosahedral three-fold axes. The contacting residues of capsomer A are mainly distributed in VR-VIII. The residue $Y588e_{AAV9P31-A}$ of capsomer A has close contacts with the residues $Q112_{Car4}/H114_{Car4}/V141_{Car4}/P156_{Car4}/L217_{Car4}$ of the bound Car4 (Fig 4A). Residue $D588f_{AAV9P31-A}$ of capsomer A form salt bridges with $K143_{Car4}$ in the positively charged region of the Car4 active center (Fig 4B). Moreover, residue $S588d_{AAV9P31-A}$ is involved in the interaction with $T219_{Car4}$ (Fig 4C). $Q590_{AAV9P31-A}$ interacts with $K83_{Car4}$, $E90_{Car4}$, $T92_{Car4}$ and $T189_{Car4}$ (Fig 4D). Moreover, $Q456_{AAV9P31-A}$, $N497_{AAV9P31-B}$ and $N498_{AAV9P31-B}$ of capsomer B approaches $K83_{Car4}$, $H187_{Car4}$ and $T189_{Car4}$ of the bound Car4
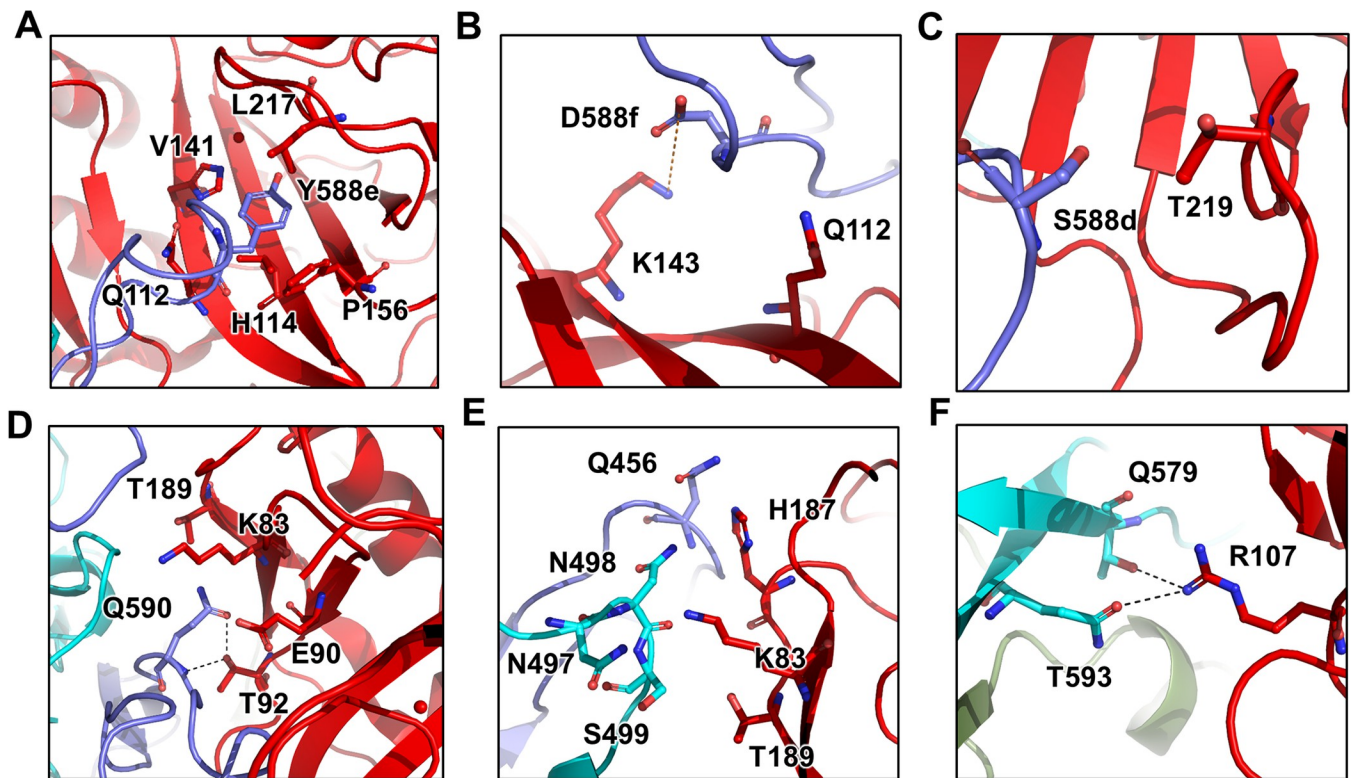
Fig 4. Detailed contacts between AAV9P31 VP3 and the bound Car4. The residues of **(A)** Y588e; **(B)** D588f; **(C)** S588d; **(D)** Q590; **(E)** Q456, N497, N498 and S499; and **(F)** Q579 and T593 that interact with Car4 are shown. Capsomer A is colored slate blue; capsomer B is colored cyan; car4 is colored red. The salt bridge is indicated by the orange dotted line; the hydrogen bonds are shown by the black dotted lines.

to stabilize the virus-receptor interaction (Fig 4E), as well as Q579$_{AAV9P31-B}$ and T593$_{AAV9P31-B}$ form hydrogen bonds with R107$_{Car4}$ (Fig 4F).

Structural comparison revealed that binding with Car4 induces conformational changes in the inserted peptides in AAV9P31 capsomers A and B (S8 Fig). Binding with Car4 induces conformational change of the inserted peptide (region I) and the loop adjacent to it (region II) in AAV9P31 capsomer A (S8A Fig). In region I, the backbone of the inserted peptide in the Car4-bound state is pulled toward Car4 from its native state by ~2.7 Å (S8B Fig). The side chains become ordered in their three-fold block reconstruction. In region II, the backbone of the loop from T451$_{AAV9P31-A}$-T460$_{AAV9P31-A}$ in the Car4-bound AAV9P31 is pushed from its original position into the capsid by ~1.8 Å (S8C Fig). In contrast, the contacts with AAV9P31 capsomers do not result in obvious shifts of the bound Car4. The bound state structure of Car4 and the individual Car4 structure (PDB: 2ZNC) share an RMSD of 1.1543 Å across all Cα atoms. A conformational change of Car4 can be observed in the loop region formed by residues G94$_{Car4}$-C98$_{Car4}$ (S6C Fig). However, because this loop region is distant from the interacting surface, the conformational change is unlikely to be related to virus-receptor interactions.

Mutagenesis study

In order to examine the impacts of the interacting residues on AAV9P31-Car4 recognition, we systematically performed alanine scanning for Car4 interface residues to assess the binding affinities with AAV9P31, employing the surface plasmon resonance (SPR) method.

Subsequently, we also conducted mutations on the residues situated at the interaction interfaces of the AAV9P31 capsid surface, aiming to elucidate their influence on AAV infection.

The residues of Car4 involved in the mutagenesis study included I70A$_{Car4}$, Q79A$_{Car4}$, K83A$_{Car4}$, T92A$_{Car4}$, I100A$_{Car4}$, R107A$_{Car4}$, Q112A$_{Car4}$, V141A$_{Car4}$, H187A$_{Car4}$, L217A$_{Car4}$ and T219A$_{Car4}$ (Figs 5B–5L and S9). Among them, the F156A$_{Car4}$ mutant could not be expressed, possibly because F156 is close to the catalytic center of Car4 and plays an essential role in the correct folding of Car4.

The results show that wt Car4 binds to AAV9P31 with an equilibrium dissociation constant (K_D) value of 106 nM (Fig 5A and S3 Table), and cannot interact with AAV9 (S11 Fig). All mutants of Car4 showed attenuated binding affinities with AAV9P31. Among them, K83$_{Car4}$, I100$_{Car4}$, R107$_{Car4}$ and H187$_{Car4}$ generated decreased RU values in SPR (Fig 5D, 5F, 5G and 5J), which is consistent with their interactions with AAV9P31 engaged by their large side chains. The replacements of Q112$_{Car4}$ and L217$_{Car4}$ as alanine residues decreased the interaction with the hydrophobic side chain of Y588e$_{AAV9P31}$, resulting in almost nondetectable response curves in SPR (Fig 5H and 5K). It is likely that the T219$_{Car4}$ and S588d$_{AAV9P31}$ interactions were also disrupted by the mutation (Fig 5L). Moreover, the mutants I70A$_{Car4}$, Q79A$_{Car4}$ and T92A$_{Car4}$ modestly attenuated the binding affinity with AAV9P31 (K_D values were 743nM, 292 nM and 379 nM, respectively) (Fig 5B, 5C and 5E, and S3 Table).

We also substituted the AAV9P31 capsid residues on the interface with alanine residues and tested the transduction activities of the mutated viruses. The results revealed a notable over 50% reduction in infection for mutants Q579A$_{AAV9P31}$, S588dA$_{AAV9P31}$, Q590A$_{AAV9P31}$, and T593A$_{AAV9P31}$ compared to the wild-type AAV9P31. Additionally, mutants N497A-N498A$_{AAV9P31}$, D588fA$_{AAV9P31}$, and Y588eA$_{AAV9P31}$ demonstrated a complete loss of cell infection capability (S10 Fig). These results are consistent with structural observations that these seven AAV9P31 capsid residues form extensive intermolecular contacts with T92, R107, K143, P156, H187, T189, L217 and T219 in Car4 to stabilize the AAV9P31-Car4 interaction.

Interactions of AAV9P31 with human carbonic anhydrase IV

In mammals, carbonic anhydrases (CAs) belong to a single gene family known as α-Cas, which consists of 16 different isoforms, 13 of which (CA I, II, III, IV, VA, VB, VI, VII, IX, XII, XIII, XIV, and XV) are enzymatically active [29]. Among them, CA IV (Car4) is a GPI-linked membrane bound protein initially purified from bovine lung [30] and also found in the brain [31], kidney [32], heart [33], eye [34], and erythrocytes [35] that is responsible for the hydration of CO_2. Because Car4 molecules are conserved in their structures and sequences throughout vertebrates (including mice, nonhuman primates and humans [23,36]) (Fig 6A–6E), we speculated that human Car4 (hCar4) may also bind AAV9P31 similar to *Mus musculus* Car4. However, the SPR results showed that wt hCar4 did not show detectable binding with AAV9P31 (Fig 6F), indicating that the potential application of AAV9P31 in humans might need further optimization, particularly in its interface with Car4.

Sequence alignments of *Car4* in *Mus musculus*, *Homo sapiens* and *rhesus macaque* indicated several key nonconserved residues that are involved in or close to the AAV9P31-Car4 interface (Fig 6A). We next mutated these residues in Car4 to their counterparts in hCar4 and measured their binding affinities with AAV9P31 by SPR. These mutants include three single residue mutations, V72S$_{Car4}$, E90M$_{Car4}$ and H187E$_{Car4}$, as well as two short peptide mutations, Mut-1$_{Car4}$ and Mut-2$_{Car4}$ (Fig 6A). In sharp contrast to the nondetectable binding of wt hCar4 with AAV9P31, all five mutants retained binding (Fig 6G–6K). The mutant V72S$_{Car4}$ exhibited binding to AAV9P31 with a K_D value of 60.7 nM, which is even higher than the binding of wt Car4 with AAV9P31 (Fig 6G and S3 Table). Because V72$_{Car4}$ has a hydrophobic side chain,
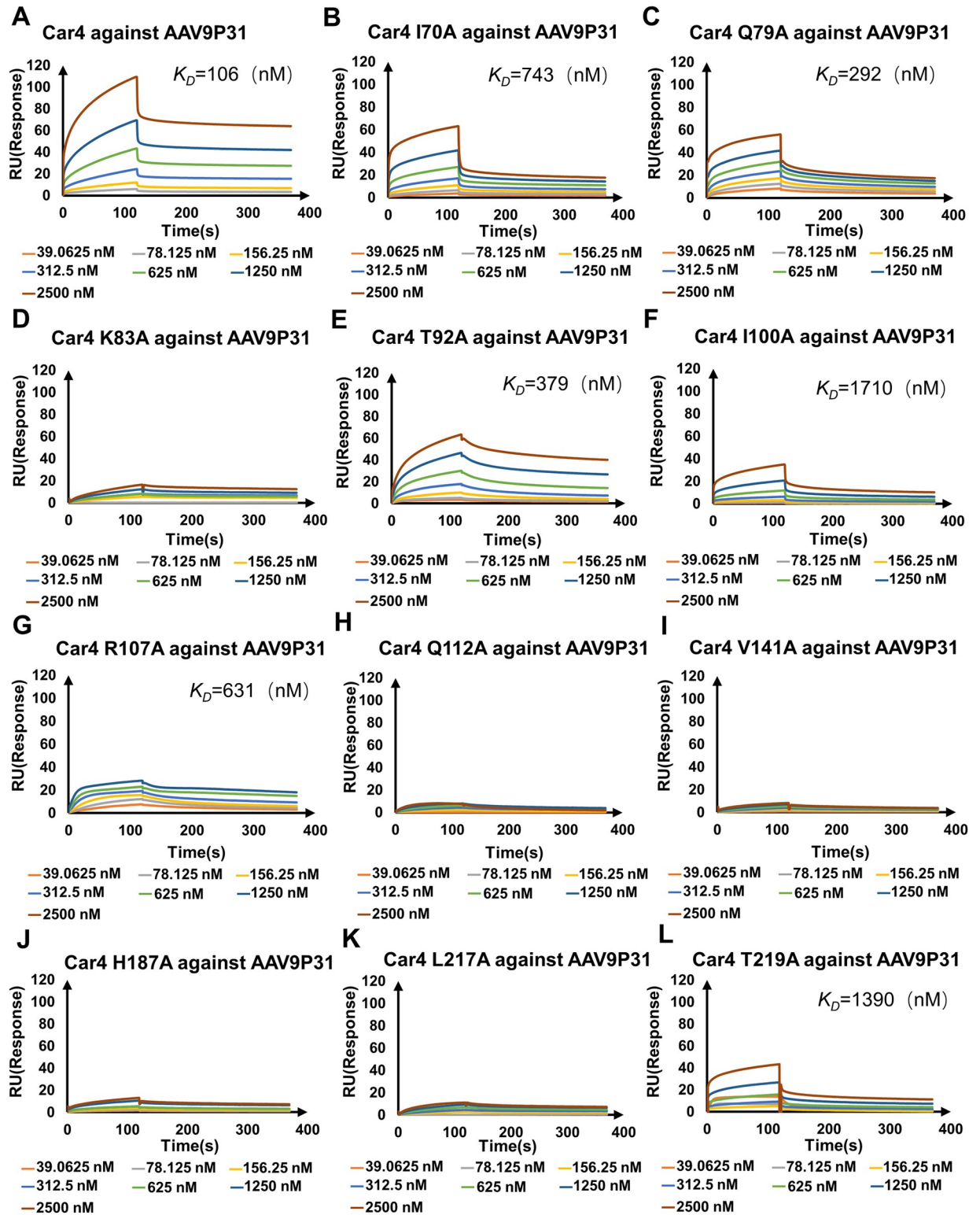
Fig 5. Mutagenesis study of Car4 for AAV9P31 binding assays. (A)-(L) Wild-type Car4 and 11 mutants were tested for binding capability to the AAV9P31 capsid by BIAcore 8K sensorgrams. The concentrations of the analytes are indicated with different colors in each panel. RU, resonance units.

https://doi.org/10.1371/journal.ppat.1011953.g005
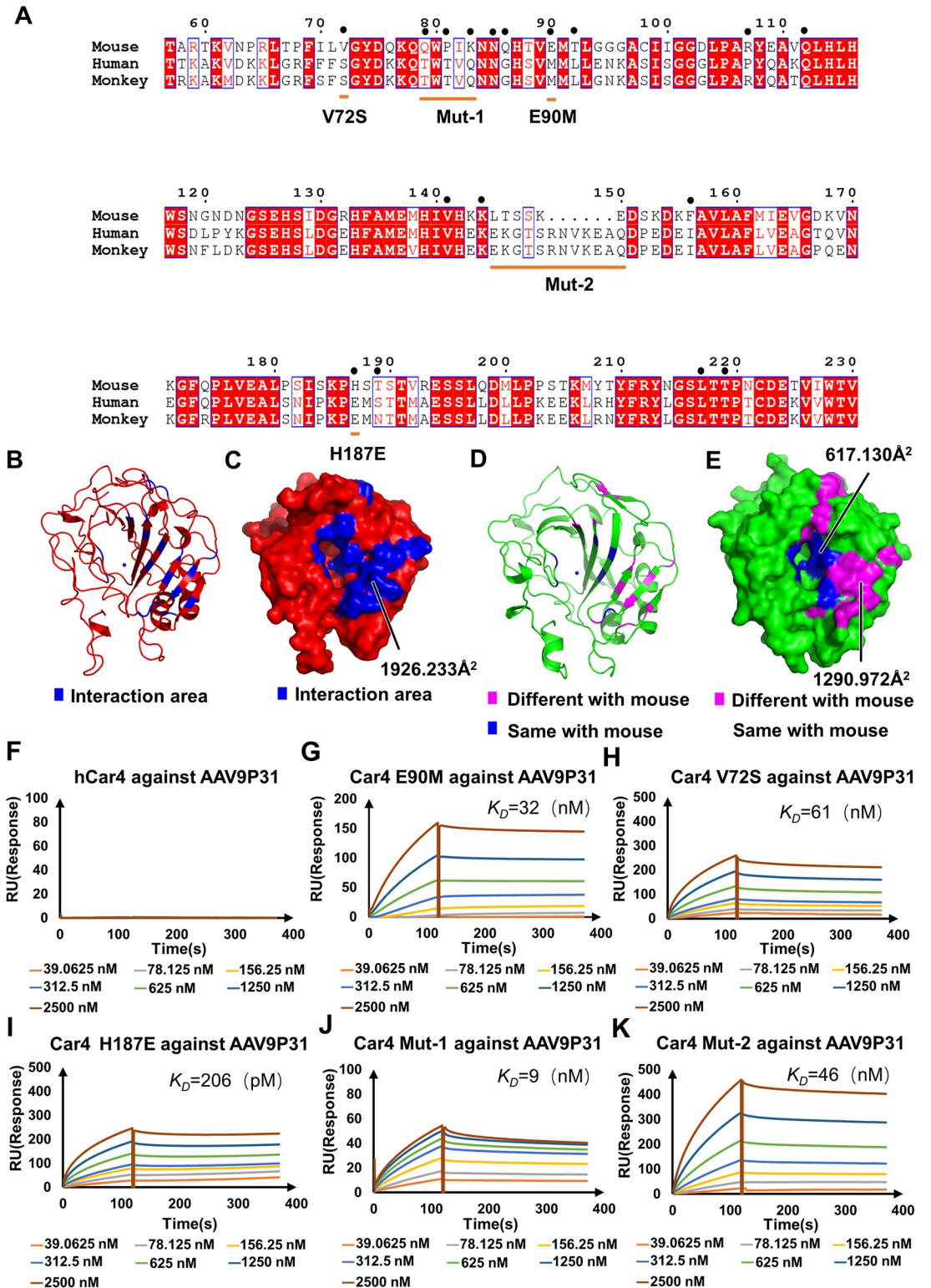
Fig 6. Car4 comparisons among *Mus musculus*, *Homo sapiens* and *Rhesus macaque*. (A) Sequence comparison among Car4 ofmice (T57 to V221), humans (T58 to V237) and monkeys (T61 to V240). The mutagenesis sites are shown by orange lines; the interacting residues on Car4 are indicated by large black dots. The red high light marks the most conserved region; yellow lines indicate the site mutations from mouse to human. The structures of Car4 (red, PDB: 2ZNC) and hCar4 (green, PDB: 1ZNC) are shown in cartoon **(B), (D)** and surface **(C), (E)** representation. The specific residues where AAV9P31 interacts with Car4 are

colored blue while the different residues on hCar4 are colored magenta. Binding assays of wild-type hCar4 and Car4 mutants (V72S, E90M, H187E, Mut-1, Mut-2) with AAV9P31 in BIAcore 8K sensorgrams are shown in (F)-(K). Concentrations are presented in different colors. The K_D values are available in S3 Table.

https://doi.org/10.1371/journal.ppat.1011953.g006

changing $V72_{Car4}$ to a serine would increase its interaction with the hydrophilic side chain of $Q456_{AAV9P31-B}$. Moreover, $E90M_{Car4}$ resulted in a highly improved binding affinity with K_D value of 32.3 nM, possibly by introducing more hydrogen bonds with $Q590_{AAV9P31}$ (Fig 6H and S3 Table). The greatest increase in binding to AAV9P31 was observed with the mutant $H187E_{Car4}$, which resulted in an ~10^3 fold increase in binding affinity with a K_D value of 206 pM (Fig 6I and S3 Table). We hypothesize that the mutation of $H187_{Car4}$ to a glutamate residue may provide improved interactions with $G455_{AAV9P31-B}$, $Q456_{AAV9P31-B}$ and $N498_{AAV9P31-B}$. Furthermore, two peptide mutants, $Mut-1_{Car4}$ and $Mut-2_{Car4}$, also increased the binding affinity with AAV9P31 (K_D = 45.9 nM and 8.7 nM, respectively) (Fig 6J, 6K and S3 Table). The inserted peptide of $Mut-2_{Car4}$ is near the protrusions surrounding the 3-fold axis of AAV9P31, which might form more interactions with the capsid.

Meanwhile, non-conserved residues engaged in Car4 binding underwent mutations in hCar4 to align with their counterparts in Car4. This includes $S72V_{hCar4}$, $M90E_{hCar4}$, $E187H_{hCar4}$, and $Mut-1_{hCar4}$. Notably, none of the four mutants exhibited interactions with AAV9P31, as evidenced by SPR experiments (S12 Fig). The reason why AAV9P31 cannot bind to hCar4 may be more complicated than the influence of these counterpart residues.

Discussion

Recognition of the specific receptor is a key determinant for AAV infection and understanding the mechanism of the AAV-receptor provides valuable information for further optimization of AAV that could be used in gene therapies. In a set of previous works, the cryo-EM structures of AAVR in complex with AAV1 [16], AAV2 [15,37,38], AAV5 [16,39], AAV9 [20], AAV-PHP.eB [20] and AAVGo.1 [40] were studied. In addition to recognition by AAVR, AAVs require more specific receptors (or entry factors) for infection within the CNS, particularly for passing through the BBB. In recent years, LY6A [18], Car4 and LY6C [36] were found to be essential for allowing recombinant AAV to pass through the BBB in mouse models. In this study, we determined the structures of AAV9P31 alone or in complex with Car4. Consistent with the functional experiments, the residues $Q112_{Car4}$, $V141_{Car4}$, $H187_{Car4}$, and $L217_{Car4}$ along with $N498_{AAV9P31-B}$ and $Y588e_{AAV9P31-A}$ at the interface are essential for virus-receptor binding, forming hydrogen bonds and salt bridges. The inserted peptide in the AAV9P31 VR-VIII loop is very important for receptor binding. As a result, the interfaces offer a wide choice of residues to mutate to potentially increase the efficiency of BBB crossing.

The current design of AAV capsids targeting the CNS depends on several screening strategies, M-CREATE [10] and TRACER [12], and mainly focuses on the Q588-A589 insertion in AAV9 VP3. Such strategies, similar to the successful improvement of AAV9 in mice for CNS targeting, remain uncertain of success in nonhuman primates [41,42]. We also demonstrated that although Car4 in humans and mice is conserved in sequence and structure, AAV9P31 cannot biochemically bind hCar4 *in vitro*, which further indicates that the novel engineered AAV capsid variants generated from current directed evolution strategies are still largely limited in terms of host species. However, several hCar4-derived mutations on Car4 presented improved binding affinity against AAV9P31. In particular, an H-to-E mutation at position 187 in Car4 resulted in a 10^3-fold increase in binding. Because $H187_{Car4}$ interacts with $N498_{AAV9P31-B}$, $G455_{AAV9P31-B}$ and $Q456_{AAV9P31-B}$ on AAV9P31 VP3 capsomers, it is conceivable that the modifications on these three VP3 residues to provide improved contacts with

$H187_{Car4}$ allow the AAV9P31 variant to be recognized by hCar4. From a structural standpoint, valuable information is obtained by superimposing hCar4 onto Car4 in the AAV9P31 bound state. It is observed that $Q590_{AAV9P31}$ approaches a non-conserved region of hCar4, potentially leading to clashes with $T58_{hCar4}$, $Q60_{hCar4}$, and $L69_{hCar4}$ (S13 Fig). Consequently, $Q590_{AAV9P31}$ represents a key point for AAV modification that can be employed in primates or humans.

Unlike the clearly elucidated of AAV-AAVR interaction, the binding between novel cellular receptors and engineered AAVs with 7-mer insertions occurs asymmetrically at 3-fold axes on the capsids [20,21]. This is a major obstacle in reconstructing the binding receptors located at the icosahedral axes of virus particles. A set of cryo-EM reconstruction methodologies have been investigated to overcome this obstacle, including focused classification to determine the structure of transferrin receptor bound with canine parvovirus [43] and symmetry-relaxation to analyze the interaction of coxsackievirus B3 (CVB3) with coxsackie and adenovirus receptor (CAR) inserted in nanodiscs [44]. In this study, we extended the application of the block-based reconstruction (BBR) [26,45] method, which was originally developed to improve the local resolution for large-scale particles, to study the asymmetric virus-receptor binding mode. The success of the structural study of the AAV9P31-Car4 complex by the BBR method presents an important solution for asymmetric receptor binding on icosahedral viruses.

In summary, the atomic structure of the AAV9P31-Car4 complex expands our knowledge of the molecular mechanism of AAV BBBcrossing. The precise virus–receptor interactions revealed in this study may facilitate the design and optimization of recombind AAV9 vectors by pinpointing specific engineerable candidate residues to produce particles with both higher efficiency for BBB crossing and the ability to cross species from mouse to human.

Materials and methods

Virus production and purification

Triple-plasmid transfection using polyethyleneimine reagent (PEIMAX) (No. 24765, Polysciences, USA) was used to produce recombinant AAV9P31 according to a previously reported protocol [16]. The pAAV9P31-GFP, pRepCap encoding AAV9P31 or mutants virus protein, and pHelper plasmids were cotransfected into HEK293T cells. For the large-scale production of AAVs, cells were seeded in 150 mm dishes at a density of 1×10^7 cells/dish for 24 hr prior to transfection and transfected with 12 μg of pHelper plasmid, 8 μg of AAV9P31 pRepCap plasmids, and 5 μg of pAAV9P31-GFP plasmids at 70% confluency. At 72 hr. post-transfection, cells were harvested by centrifugation at $500 \times g$ at 4˚C for 5 min. The pellet was collected and resuspended in lysis buffer containing 50 mM Tris-HCl, pH 8.0, 150 mM NaCl. The suspension was subjected to three freeze-thaw cycles in dry ice/ethanol and a 37˚C water bath. Then, benzonase (100 units/ml) and 0.5% sodium deoxycholate were added, and the cell suspension was incubated for 1 hour at 37˚C. Following centrifugation at $5,000 \times g$ for 20 min at 4˚C, the supernatant containing the AAV9P31 crude lysate was collected. For AAV9P31 infection assay, AAV crude lysate genome copy titers were determined by real-time quantitative PCR (qPCR) using primers specific for the GFP gene sequences. The primers used were as follows: qpcr-GFP-F, TCTTCAAGTCCGCCATGCC; qpcr-GFP-R, TGTCGCCCTCGAACTTCAC.

The crude lysate was diluted with 10 mM Tris-HCl (pH 8.0) buffer to a final volume of 10 ml and then bottom loaded on a discontinuous gradient of 15%, 25%, 40% and 60% iodixanol in a 39 ml ultracentrifuge tube (Quick-Seal 342414, Beckman, USA). After ultracentrifugation at $350,000 \times g$ at 18˚C for 1 hr, 3 ml fractions in the 40% lower layer and 0.5 ml of the 60% upper layer were collected. The viral titers in each fraction were determined by negative staining. The fractions with the highest titers were desalted using a 100 kDa cutoff ultrafiltration

tube (15 ml; Millipore, USA), and the buffer was changed to PBS. Purified AAV9P31 was stored at -80˚C until use.

Purification of Car4

DNA encoding the truncated Car4 (22–277) (NCBI Gene ID: 12351) with an N-terminal GST-tag in a pGEX-6p-1 vector was transformed into *Escherichia coli* BL21 (DE3) cells and cultured in Luria-Bertani (LB) medium containing 100 μg/ml ampicillin at 37˚C. When the OD_{600} of the culture reached 0.6, protein expression was induced by the addition of both isopropyl β-D-thiogalactoside (IPTG) and zinc sulphate ($ZnSO_4$) at a final concentration of 0.5 mM, followed by another 18 hr. of cell culture. The cells were harvested by centrifugation at 4,000 rpm for 15 min. The pellet was resuspended in lysis buffer (20 mM HEPES, pH 8.0; 150 mM NaCl) and then homogenized by sonication. The fusion protein was then isolated from its crude lysate by GST affinity chromatography (Qiagen, Holland) and digested overnight by HRV 3C Protease at 16˚C without shaking in lysis buffer. The eluted protein was further purified by size exclusion using Superdex 75 (GE Healthcare, USA). Mutated Car4 constructs were generated using the Fast Mutagenesis System (Transgene, China), and the mutated proteins were purified as described above. The purified proteins were concentrated to 2 mg/ml for storage at -80˚C until use.

Sample preparation and cryo-EM data collection

A 5 μl aliquot of AAV9P31 was loaded onto a glow-discharged, carbon-coated copper grid (Cu 1.2/1.3+C, 300 mesh; Quantifoil) bearing an ultrathin layer of carbon and incubated for two minutes. The liquid was then sucked away by a filter and 3 μl of Car4 was loaded on the same grid, and incubated for another five minutes with 100% humidity. The grid was then blotted for 4.5 s with a blot force of 0 in 100% relative humidity and plunge-frozen in liquid ethane using a Vitrobot Mark IV (FEI, USA). Cryo-EM data were collected with a 300 kV Titan Krios electron microscope (FEI, USA) and a K3 direct electron detector (FEI, USA). A series of micrographs were collected as movies and recorded with -2.2 to -0.5 μm defocus at a calibrated magnification of 105,000×, resulting in a pixel size of 0.8433 Å per pixel. Statistics for data collection and refinement are summarized in S1 Table.

Image processing and three-dimensional icosahedral reconstruction

After data collection, each movie was motion corrected and dose-weighted micrographs were abtained by MotionCor2 [46]. The contrast transfer function parameters were estimated by CTFFIND4 [47]. Then all micrographs with CTF fitting resolution > 4 Å were excluded and 6,068 good images were obtained for subsequent data processing. Particles were auto picked and extracted in Relion-3.1.2 [48,49]. After multiple rounds of 2D classification and 3D classification with C1 symmetry, 226,724 good particles were selected and subjected to 3D autorefinement with I1 symmetry yielding a reconstruction with a resolution of 2.13 Å. To push a higher resolution, we further used global and local CTF refinement to refine the beam tilt and per-particle CTF and brought the resolution to 1.89 Å. The final reconstruction used Ewald sphere correction with negative curvature yielding a reconstruction with a resolution of 1.76 Å. AAV9P31 particles without Car4 were reconstructed and refined in CryoSPARC-4.0.3 [50]. Following the same steps as above, the final reconstruction ended in 1.76 Å resolution.

Sub-particles classification and reconstruction in the 3-axis region

Block-based reconstruction was used to extract blocks near the 3-fold axes and icosahedral symmetry was applied [26]. The coordinates of a sub-particle were first determined in USCF

Chimera. After employing symmetry expansion and dropping blocks located outside the micrographs, 13,604,676 blocks were selected and re-extracted with a smaller box size (160 pixels). Blocks were reconstructed with the "relion_reconstruct" command to generate a reference map and the reference was low pass filtered to 60 Å for one round of 3D classification which applied C1 symmetry without alignment. Sixteen classes were generated, six of which included notable receptor density. Those classes contained receptors that are similar in structure but the rotational difference between them is approximately 120°. Blocks with the same receptor binding site were combined and subjected to 3D autorefinement with C1 symmetry, yielding reconstruction of Car4-VP3 complexes with resolutions of 2.59 Å, 2.59 Å and 2.28 Å, respectively.

Model building and refinement

All maps were built in Coot and refined in Phenix real space refine [51,52]. The AAV9 cryo-EM structure (PDB:7WJW) and Car4 crystal structure (PDB:2ZNC) were used as references for AAV9P31 and AAV9P31-Car4 model building. All figures were prepared in Chimera, ChimeraX and PyMOL [53–55].

Surface plasmon resonance (SPR)

SPR analyses were carried out using a BIAcore 8K (GE Healthcare, USA) with a flow rate of 30 μl/min at 25°C in PBST buffer. AAV9P31 particles suspended in sodium acetate buffer (pH 4.0) were immobilized on a CM5 sensor chip by amide coupling. Different concentrations of the recombinant WT or mutated Car4 proteins flowed over the chip and between each sample we used glycine-HCl (10mM glycine, pH 2.0) for chip surface regeneration. The binding affinity was determined, and curves were generated by BIAEvaluation software (GE Healthcare, USA).

AAV infection assays

Recombinant AAV vectors carrying a GFP expression cassette were used to evaluate viral transduction efficiency. Twenty-four hours prior to infection, HEK293T cells were seeded at 80% confluency in a 10cm plate and maintained in Dulbecco's modified Eagle's medium (DMEM) supplemented with 10% FBS and penicillin-streptomycin (100 U ml^{-1}) at 37°C in 5% CO_2. DNA encoding the full length Car4 (NCBI Gene ID: 12351) with a C-terminal 3 × Flag-tag was inserted in a pBMCL vector, which was a gift from Prof. Lei Chen in Peking University. The full length Car4 was transiently expressed in HEK293T cells by transfecting with 16 μg of plasmid DNA. Twelve hours later, Car4-expressing cells were transferred to 96-well plates with 2×10^4 per well and maintained in DMEM supplemented with 10% FBS, penicillin-streptomycin (100 U ml^{-1}) at 37°C in 5% CO_2. Cells were infected with AAV9P31 or mutants at an MOI of 1×10^6 viral genome (vg) per cell in triplicate. At 48 h post-infection, GFP expression levels were measured by flow cytometry using a BD LSRFortessa analyzer (BD Biosciences, USA).

Supporting information

S1 Fig. Resolution of AAV9P31 and AAV9P31-Car4. Fourier shell correlation (FSC) of the final 3D reconstruction following gold standard refinement using RELION [48,49]. The resolutions corresponding to an FSC of 0.143 are shown for **(A)** unbound AAV9P31, **(C)** AAV9P31-Car4 complex and **(E)** 3-fold block of AAV9P31-Car4. **(B), (D), (F)** The surface of

the maps is colored from red to blue indicating the different local resolutions.
(PDF)

S2 Fig. The key loop density of reconstructed AAV9P31. The unbound AAV9P31 **(A)** VR-I, **(B)** VR-III, **(C)** VR-IV and **(D)** VR-V fragment stick models fitted into electron density. VR-1: counter level = 1.0σ, carve = 1.5; VR-III: counter level = 2.0σ, carve = 1.5; VR-IV: counter level = 1.0σ, carve = 1.5; VR-V: counter level = 2.0σ, carve = 1.5. Electron density is presented as sweat mesh.
(PDF)

S3 Fig. Structure and sequence alignment of AAV9 and AAV9P31. (A) The cartoon models of AAV9(gray) and AAV9P31(cyan) are aligned together. The red box shows the structural difference in variable region VIII between AAV9 and AAV9P31. The 5-, 3- and 2-fold icosahedral axes of symmetry are indicated with a pentagon, triangles, and an oval, respectively. **(B)** Sequence alignment of AAV9 and AAV9P31 in variable region VIII. The inserted peptide residues are highlighted in bright yellow. **(C)** The stick model of the inserted peptide (pink) in variable region VIII in AAV9P31 electron density.
(PDF)

S4 Fig. Cryo-EM data-processing pipeline for the AAV9P31-Car4 complex. Overview of the cryo-EM data processing pipeline in RELION [48,49]. **(A)** Cryo-EM sample data collected in a 300 kV Titan Krios electron microscope with 0.8433 Å per pixel. **(B)** The micrographs are selected with the CTF estimated maximum resolution (threshold: <4.0 Å). **(C)** Particles are automatically picked from micrographs. **(D)** The particles selected by multiple rounds of 2D classifications. **(E)** Multiple rounds of 3D classifications with C1 symmetry, after which two classes were selected for the 3D refinement. **(F)** The AAV9P31-Car4 complex was reconstructed with I1 symmetry after local CTF refinement. The selected classes are colored gray and unselected classes are colored white.
(PDF)

S5 Fig. Cryo-EM data-processing pipeline for AAV9P31-Car4 3-fold blocks. Overview of the cryo-EM data processing pipeline of block-based reconstruction in RELION [48,49]. **(A)** The I1 reconstructed 3D map of the AAV9P31-Car4 complex. **(B)** Blocks are isolated from the icosahedral 3-fold axes by symmetry expansion. **(C)** 3D classifications of 3-fold blocks. **(D)-(F)** Three different classes are refined in C1 symmetry. Car4 electron density presented as blue; noise presented as red.
(PDF)

S6 Fig. Structural comparison between bound and unbound Car4. (A) The overall structures of the bound and unbound (PDB:2ZNC) states of Car4. **(B)** The newly solved loop region is enlarged, and shown in stick representarion in our electronic density. The red ring shows that the bound state Car4 swings considerably compared with the unbound state. The unbound state Car4 is colored light blue and the bound state is colored orange. The mesh is colored gray. **(C)** The magnified figure of the red circle in **(A)**. Loops of bound and unbound state Car4 are shown in stick representation.
(PDF)

S7 Fig. Density of key residues at AAV9P31-Car4 interfaces. Left side of the panel shows the key interacting region in bound state AAV9P31 **(A)** 586–591, **(B)** 455–459, **(C)** 495–501 and **(D)** 590–592 fragments' stick models fitted into electron density. The right side of the panel shows the key interacting region in Car4 **(E)** 79–86, **(F)** 111–115, **(G)** 186–190 and **(H)** 154–156 fragment stick models fitted into electron density. Electron density is presented as gray

mesh. Capsomer A is shown in blue-slate; capsomer B is shown in cyan; Car4 is shown in red.
(PDF)

S8 Fig. Conformational changes in the AAV9P31 capsid following Car4 attachment. (A)
The structural change in the AAV9P31 capsid between the Car4-bound (red) and unbound
AAV9P31 (gray) states, shown in cartoon representation. The approximate inner and outer
boundaries of the shell are marked by two solid arcs. The icosahedral three-fold axis is indi-
cated at its approximate position by the dotted line. Car4 is shown in red. **(B)** and **(C)** The two
major conformational changes in regions I and II boxed in **(A)** are enlarged in **(B)** and **(C)**,
respectively. Residues with conformational changes in Car4 and the AAV9P31 capsid are
shown in stick representation with the same colors as in the cartoon diagrams.
(PDF)

S9 Fig. All the yield proteins were tested by SDS–PAGE. (A) The peak in gel filtration chro-
matography by Superdex 75 (GE). **(B)-(F)** SDS–PAGE of mutants of Car4, hCar4, wild-type
Car4 and hCar4. The molecular weights are labeled on each panel. Car4 or hCar4 is approxi-
mately 35 kDa.
(PDF)

**S10 Fig. AAV9P31 viral particles bearing capsid mutations at the receptor-binding sites
impacted viral infection.** HEK293T transduced by full length Car4 were infected with mutant
AAV9P31 at an MOI of 1×10^6 vg cell^{-1}. GFP expression was determined 48 h post-transduc-
tion by flow cytometry. The percentages of cells infected by AAV9P31 mutants are plotted as
means ± standard errors (n = 3).
(PDF)

S11 Fig. The binding affinity between Car4 and AAV9. Wild-type Car4 was tested for bind-
ing capability to the AAV9 by BIAcore 8K sensorgrams. The concentrations of the analytes are
indicated with different colors in each panel. RU, resonance units.
(PDF)

S12 Fig. AAV9P31 and hCar4 mutants binding assay. (A)-(D) Human Car4 mutants were
tested for binding capability to the AAV9p31 capsid by BIAcore 8K sensorgrams. The concen-
trations of the analytes are indicated with different colors in each panel. RU, resonance units.
(PDF)

S13 Fig. Superposition of hCar4 and Car4 in the AAV9P31 bound state. (A) hCar4 is super-
posed onto Car4 in the AAV9P31-Car4 complex. hCar4 is colored wheat; Car4 is colored grey;
AAV9P31 virus proteins are colored pink. **(B)** Magnification of the red box in the left panel to
highlight the details of the residues. The distances between the residues are marked. The resi-
dues of Car4 involved in the interactions are colored limon; the counterpart residues in hCar4
are colored blue; Q590$_{AAV9P31}$ is colored in red. All these residues are shown as sticks.
(PDF)

S1 Table. Cryo-EM data collection, refinement and validation statistics.
(PDF)

S2 Table. Interactions between AAV9P31 and Car4.
(PDF)

S3 Table. Surface plasma resonance (SPR) experiment.
(PDF)

S1 Data. Excel spreadsheet containing, in separate sheets, the underlying numerical data and statistical analysis for figure panels Figs 5A, 5B, 5C, 5D, 5E, 5F, 5G, 5H, 5I, 5J, 5K, 5L, 6F, 6G, 6H, 6I, 6J, 6K, S10, S11, S12A, S12B, S12C and S12D.
(XLSX)

Acknowledgments

Author Contributions

Conceptualization: Ran Zhang, Guangxue Xu, Zhiyong Lou.

Data curation: Ran Zhang, Yixiao Liu, Fengxi Yu, Baobin Li.

Formal analysis: Ran Zhang, Yixiao Liu.

Funding acquisition: Ran Zhang, Zhiyong Lou.

Investigation: Ran Zhang, Lili Li.

Methodology: Yixiao Liu, Fengxi Yu, Guangxue Xu, Baobin Li.

Project administration: Ran Zhang, Guangxue Xu.

Supervision: Zhiyong Lou.

Writing – original draft: Ran Zhang, Yixiao Liu.

Writing – review & editing: Ran Zhang, Zhiyong Lou.

References

1. Zinn E, Vandenberghe LH. Adeno-associated virus: fit to serve. Curr Opin Virol. 2014; 8:90–7. https://doi.org/10.1016/j.coviro.2014.07.008 PMID: 25128609

2. Kotterman MA, Schaffer DV. Engineering adeno-associated viruses for clinical gene therapy. Nat Rev Genet. 2014; 15(7):445–51. https://doi.org/10.1038/nrg3742 PMID: 24840552

3. Jacobson SG, Cideciyan AV, Ratnakaram R, Heon E, Schwartz SB, Roman AJ, et al. Gene therapy for leber congenital amaurosis caused by RPE65 mutations: safety and efficacy in 15 children and adults followed up to 3 years. Archives of ophthalmology (Chicago, Ill: 1960). 2012; 130(1):9–24. https://doi.org/10.1001/archophthalmol.2011.298 PMID: 21911650

4. Maguire AM, Russell S, Wellman JA, Chung DC, Yu ZF, Tillman A, et al. Efficacy, Safety, and Durability of Voretigene Neparvovec-rzyl in RPE65 Mutation-Associated Inherited Retinal Dystrophy: Results of Phase 1 and 3 Trials. Ophthalmology. 2019; 126(9):1273–85. https://doi.org/10.1016/j.ophtha.2019.06.017 PMID: 31443789

5. Zolgensma—one-time gene therapy for spinal muscular atrophy. The Medical letter on drugs and therapeutics. 2019; 61(1577):113–4. PMID: 31381549

6. Blair HA. Valoctocogene Roxaparvovec: First Approval. Drugs. 2022; 82(14):1505–10. https://doi.org/10.1007/s40265-022-01788-y PMID: 36214970

7. Hoy SM. Delandistrogene Moxeparvovec: First Approval. Drugs. 2023; 83(14):1323–9. https://doi.org/10.1007/s40265-023-01929-x PMID: 37566211

8. Kang L, Jin S, Wang J, Lv Z, Xin C, Tan C, et al. AAV vectors applied to the treatment of CNS disorders: Clinical status and challenges. Journal of controlled release: official journal of the Controlled Release Society. 2023; 355:458–73. https://doi.org/10.1016/j.jconrel.2023.01.067 PMID: 36736907

9. Morris JA, Boshoff CH, Schor NF, Wong LM, Gao G, Davidson BL. Next-generation strategies for gene-targeted therapies of central nervous system disorders: A workshop summary. Mol Ther. 2021; 29 (12):3332–44. https://doi.org/10.1016/j.ymthe.2021.09.010 PMID: 34547463

10. Deverman BE, Pravdo PL, Simpson BP, Kumar SR, Chan KY, Banerjee A, et al. Cre-dependent selection yields AAV variants for widespread gene transfer to the adult brain. Nat Biotechnol. 2016; 34 (2):204–9. https://doi.org/10.1038/nbt.3440 PMID: 26829320

11. Chan KY, Jang MJ, Yoo BB, Greenbaum A, Ravi N, Wu WL, et al. Engineered AAVs for efficient noninvasive gene delivery to the central and peripheral nervous systems. Nat Neurosci. 2017; 20(8):1172–9. https://doi.org/10.1038/nn.4593 PMID: 28671695

12. Nonnenmacher M, Wang W, Child MA, Ren XQ, Huang C, Ren AZ, et al. Rapid evolution of blood-brain-barrier-penetrating AAV capsids by RNA-driven biopanning. Mol Ther Methods Clin Dev. 2021; 20:366–78. https://doi.org/10.1016/j.omtm.2020.12.006 PMID: 33553485

13. Ibraghimov-Beskrovnaya O, Bukanov NO, Donohue LC, Dackowski WR, Klinger KW, Landes GM. Strong homophilic interactions of the Ig-like domains of polycystin-1, the protein product of an autosomal dominant polycystic kidney disease gene, PKD1. Hum Mol Genet. 2000; 9(11):1641–9. https://doi.org/10.1093/hmg/9.11.1641 PMID: 10861291

14. Pillay S, Meyer NL, Puschnik AS, Davulcu O, Diep J, Ishikawa Y, et al. An essential receptor for adeno-associated virus infection. Nature. 2016; 530(7588):108–12. https://doi.org/10.1038/nature16465 PMID: 26814968

15. Zhang R, Cao L, Cui M, Sun Z, Hu M, Zhang R, et al. Adeno-associated virus 2 bound to its cellular receptor AAVR. Nat Microbiol. 2019.

16. Zhang R, Xu G, Cao L, Sun Z, He Y, Cui M, et al. Divergent engagements between adeno-associated viruses with their cellular receptor AAVR. Nature communications. 2019; 10(1):3760. https://doi.org/10.1038/s41467-019-11668-x PMID: 31434885

17. Batista AR, King OD, Reardon CP, Davis C, Shankaracharya Philip V, et al. Ly6a Differential Expression in Blood-Brain Barrier Is Responsible for Strain Specific Central Nervous System Transduction Profile of AAV-PHP.B. Human gene therapy. 2020; 31(1–2):90–102. https://doi.org/10.1089/hum.2019.186 PMID: 31696742

18. Hordeaux J, Yuan Y, Clark PM, Wang Q, Martino RA, Sims JJ, et al. The GPI-Linked Protein LY6A Drives AAV-PHP.B Transport across the Blood-Brain Barrier. Mol Ther. 2019; 27(5):912–21. https://doi.org/10.1016/j.ymthe.2019.02.013 PMID: 30819613

19. Huang Q, Chan KY, Tobey IG, Chan YA, Poterba T, Boutros CL, et al. Delivering genes across the blood-brain barrier: LY6A, a novel cellular receptor for AAV-PHP.B capsids. PloS one. 2019; 14(11): e0225206. https://doi.org/10.1371/journal.pone.0225206 PMID: 31725765

20. Xu G, Zhang R, Li H, Yin K, Ma X, Lou Z. Structural basis for the neurotropic AAV9 and the engineered AAVPHP.eB recognition with cellular receptors. Mol Ther Methods Clin Dev. 2022; 26:52–60. https://doi.org/10.1016/j.omtm.2022.05.009 PMID: 35755945

21. Shay TF, Sullivan EE, Ding X, Chen X, Ravindra Kumar S, Goertsen D, et al. Primate-conserved carbonic anhydrase IV and murine-restricted LY6C1 enable blood-brain barrier crossing by engineered viral vectors. Science advances. 2023; 9(16):eadg6618. https://doi.org/10.1126/sciadv.adg6618 PMID: 37075114

22. Ghandour MS, Langley OK, Zhu XL, Waheed A, Sly WS. Carbonic anhydrase IV on brain capillary endothelial cells: a marker associated with the blood-brain barrier. Proc Natl Acad Sci U S A. 1992; 89 (15):6823–7. https://doi.org/10.1073/pnas.89.15.6823 PMID: 1495971

23. Stams T, Chen Y, Boriack-Sjodin PA, Hurt JD, Liao J, May JA, et al. Structures of murine carbonic anhydrase IV and human carbonic anhydrase II complexed with brinzolamide: molecular basis of isozyme-drug discrimination. Protein science: a publication of the Protein Society. 1998; 7(3):556–63. https://doi.org/10.1002/pro.5560070303 PMID: 9541386

24. Stams T, Nair SK, Okuyama T, Waheed A, Sly WS, Christianson DW. Crystal structure of the secretory form of membrane-associated human carbonic anhydrase IV at 2.8-A resolution. Proc Natl Acad Sci U S A. 1996; 93(24):13589–94. https://doi.org/10.1073/pnas.93.24.13589 PMID: 8942978

25. Tolvanen ME, Ortutay C, Barker HR, Aspatwar A, Patrikainen M, Parkkila S. Analysis of evolution of carbonic anhydrases IV and XV reveals a rich history of gene duplications and a new group of isozymes. Bioorganic & medicinal chemistry. 2013; 21(6):1503–10. https://doi.org/10.1016/j.bmc.2012.08.060 PMID: 23022279

26. Zhu D, Wang X, Fang Q, Van Etten JL, Rossmann MG, Rao Z, et al. Pushing the resolution limit by correcting the Ewald sphere effect in single-particle Cryo-EM reconstructions. Nat Commun. 2018; 9 (1):1552. https://doi.org/10.1038/s41467-018-04051-9 PMID: 29674632

27. Zhu DJ, Wang XX, Fang QL, Van Etten JL, Rossmann MG, Rao ZH, et al. Pushing the resolution limit by correcting the Ewald sphere effect in single-particle Cryo-EM reconstructions. Nature communications. 2018; 9. https://doi.org/10.1038/s41467-018-04051-9 PMID: 29674632

28. Winn MD, Ballard CC, Cowtan KD, Dodson EJ, Emsley P, Evans PR, et al. Overview of the CCP4 suite and current developments. Acta Crystallogr D Biol Crystallogr. 2011; 67(Pt 4):235–42. https://doi.org/10.1107/S0907444910045749 PMID: 21460441

29. Pan PW, Rodriguez A, Parkkila S. A systematic quantification of carbonic anhydrase transcripts in the mouse digestive system. BMC Mol Biol. 2007; 8:22. https://doi.org/10.1186/1471-2199-8-22 PMID: 17362527

30. Whitney PL, Briggle TV. Membrane-associated carbonic anhydrase purified from bovine lung. J Biol Chem. 1982; 257(20):12056–9. PMID: 6811592

31. Brion LP, Suarez C, Zhang H, Cammer W. Up-regulation of carbonic anhydrase isozyme IV in CNS myelin of mice genetically deficient in carbonic anhydrase II. J Neurochem. 1994; 63(1):360–6. https://doi.org/10.1046/j.1471-4159.1994.63010360.x PMID: 8207439

32. Wistrand PJ. Properties of membrane-bound carbonic anhydrase. Ann N Y Acad Sci. 1984; 429:195–206. https://doi.org/10.1111/j.1749-6632.1984.tb12333.x PMID: 6430159

33. Sender S, Decker B, Fenske CD, Sly WS, Carter ND, Gros G. Localization of carbonic anhydrase IV in rat and human heart muscle. J Histochem Cytochem. 1998; 46(7):855–61. https://doi.org/10.1177/002215549804600709 PMID: 9632745

34. Hageman GS, Zhu XL, Waheed A, Sly WS. Localization of carbonic anhydrase IV in a specific capillary bed of the human eye. Proc Natl Acad Sci U S A. 1991; 88(7):2716–20. https://doi.org/10.1073/pnas.88.7.2716 PMID: 1901414

35. Wistrand PJ, Carter ND, Conroy CW, Mahieu I. Carbonic anhydrase IV activity is localized on the exterior surface of human erythrocytes. Acta Physiol Scand. 1999; 165(2):211–8. https://doi.org/10.1046/j.1365-201x.1999.00478.x PMID: 10090333

36. Shay TF, Sullivan EE, Ding X, Chen X, Kumar SR, Goertsen D, et al. Primate-conserved Carbonic Anhydrase IV and murine-restricted Ly6c1 are new targets for crossing the blood-brain barrier. bioRxiv. 2023:2023.01.12.523632.

37. Meyer NL, Hu G, Davulcu O, Xie Q, Noble AJ, Yoshioka C, et al. Structure of the gene therapy vector, adeno-associated virus with its cell receptor, AAVR. Elife. 2019; 8. https://doi.org/10.7554/eLife.44707 PMID: 31115336

38. Hu G, Silveria MA, Zane GM, Chapman MS, Stagg SM. Adeno-Associated Virus Receptor-Binding: Flexible Domains and Alternative Conformations through Cryo-Electron Tomography of Adeno-Associated Virus 2 (AAV2) and AAV5 Complexes. J Virol. 2022; 96(13):e0010622. https://doi.org/10.1128/jvi.00106-22 PMID: 35674430

39. Silveria MA, Large EE, Zane GM, White TA, Chapman MS. The Structure of an AAV5-AAVR Complex at 2.5 A Resolution: Implications for Cellular Entry and Immune Neutralization of AAV Gene Therapy Vectors. Viruses. 2020; 12(11).

40. Large EE, Silveria MA, Weerakoon O, White TA, Chapman MS. Cross-Species Permissivity: Structure of a Goat Adeno-Associated Virus and Its Complex with the Human Receptor AAVR. J Virol. 2022; 96 (24):e0148422. https://doi.org/10.1128/jvi.01484-22 PMID: 36453885

41. Hordeaux J, Wang Q, Katz N, Buza EL, Bell P, Wilson JM. The Neurotropic Properties of AAV-PHP.B Are Limited to C57BL/6J Mice. Mol Ther. 2018; 26(3):664–8. https://doi.org/10.1016/j.ymthe.2018.01.018 PMID: 29428298

42. Matsuzaki Y, Konno A, Mochizuki R, Shinohara Y, Nitta K, Okada Y, et al. Intravenous administration of the adeno-associated virus-PHP.B capsid fails to upregulate transduction efficiency in the marmoset brain. Neurosci Lett. 2018; 665:182–8. https://doi.org/10.1016/j.neulet.2017.11.049 PMID: 29175632

43. Lee H, Callaway HM, Cifuente JO, Bator CM, Parrish CR, Hafenstein SL. Transferrin receptor binds virus capsid with dynamic motion. Proc Natl Acad Sci U S A. 2019; 116(41):20462–71. https://doi.org/10.1073/pnas.1904918116 PMID: 31548398

44. Lee H, Shingler KL, Organtini LJ, Ashley RE, Makhov AM, Conway JF, et al. The novel asymmetric entry intermediate of a picornavirus captured with nanodiscs. Science advances. 2016; 2(8):e1501929. https://doi.org/10.1126/sciadv.1501929 PMID: 27574701

45. Basore K, Ma H, Kafai NM, Mackin S, Kim AS, Nelson CA, et al. Structure of Venezuelan equine encephalitis virus in complex with the LDLRAD3 receptor. Nature. 2021; 598(7882):672–6. https://doi.org/10.1038/s41586-021-03963-9 PMID: 34646020

46. Zheng SQ, Palovcak E, Armache JP, Verba KA, Cheng Y, Agard DA. MotionCor2: anisotropic correction of beam-induced motion for improved cryo-electron microscopy. Nat Methods. 2017; 14(4):331–2. https://doi.org/10.1038/nmeth.4193 PMID: 28250466

47. Mindell JA, Grigorieff N. Accurate determination of local defocus and specimen tilt in electron microscopy. J Struct Biol. 2003; 142(3):334–47. https://doi.org/10.1016/s1047-8477(03)00069-8 PMID: 12781660

48. Zivanov J, Nakane T, Forsberg BO, Kimanius D, Hagen WJ, Lindahl E, et al. New tools for automated high-resolution cryo-EM structure determination in RELION-3. Elife. 2018; 7. https://doi.org/10.7554/eLife.42166 PMID: 30412051

49. Scheres SH. RELION: implementation of a Bayesian approach to cryo-EM structure determination. J Struct Biol. 2012; 180(3):519–30. https://doi.org/10.1016/j.jsb.2012.09.006 PMID: 23000701

50. Punjani A, Rubinstein JL, Fleet DJ, Brubaker MA. cryoSPARC: algorithms for rapid unsupervised cryo-EM structure determination. Nat Methods. 2017; 14(3):290–6. https://doi.org/10.1038/nmeth.4169 PMID: 28165473

51. Adams PD, Afonine PV, Bunkoczi G, Chen VB, Davis IW, Echols N, et al. PHENIX: a comprehensive Python-based system for macromolecular structure solution. Acta Crystallogr D Biol Crystallogr. 2010; 66(Pt 2):213–21. https://doi.org/10.1107/S0907444909052925 PMID: 20124702

52. Emsley P, Cowtan K. Coot: model-building tools for molecular graphics. Acta Crystallogr D Biol Crystallogr. 2004; 60(Pt 12 Pt 1):2126–32. https://doi.org/10.1107/S0907444904019158 PMID: 15572765

53. Pettersen EF, Goddard TD, Huang CC, Couch GS, Greenblatt DM, Meng EC, et al. UCSF Chimera—a visualization system for exploratory research and analysis. J Comput Chem. 2004; 25(13):1605–12. https://doi.org/10.1002/jcc.20084 PMID: 15264254

54. Schrodinger, LLC. The PyMOL Molecular Graphics System, Version 1.8. 2015.

55. Pettersen EF, Goddard TD, Huang CC, Meng EC, Couch GS, Croll TI, et al. UCSF ChimeraX: Structure visualization for researchers, educators, and developers. Protein Sci. 2021; 30(1):70–82. https://doi.org/10.1002/pro.3943 PMID: 32881101